Volume 15
Number 6
14 February 2023
Pages 2439-2964

Nanoscale

rsc.li/nanoscale

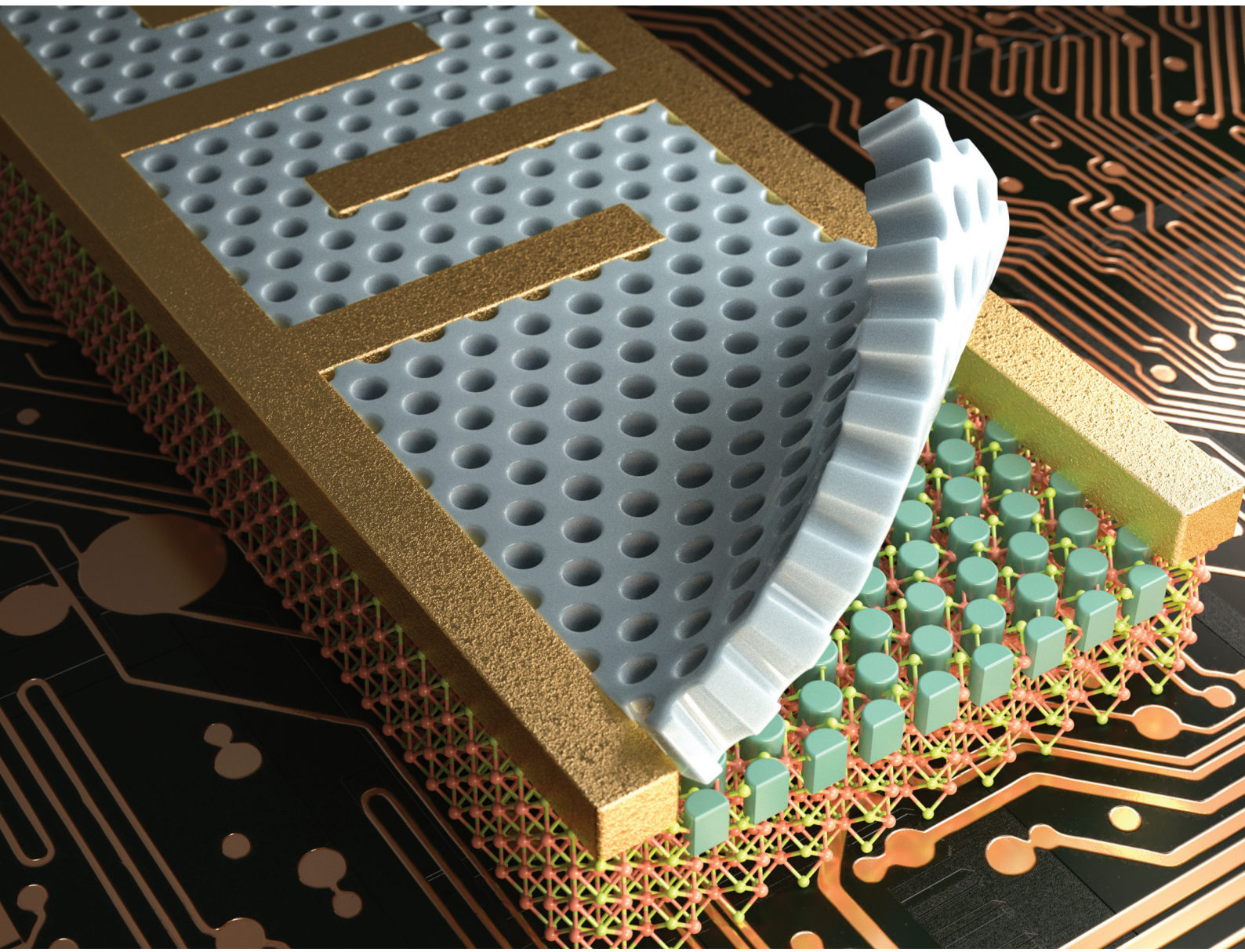

ISSN 2040-3372

ROYAL SOCIETY OF CHEMISTRY

PAPER
Joona Bang, Jihyun Kim *et al.*
Nanostructured doping of WSe_2 *via* block copolymer patterns and its self-powered photodetector application

NCNST

Nanoscale

ROYAL SOCIETY OF CHEMISTRY

PAPER

View Article Online
View Journal | View Issue

Check for updates

Cite this: *Nanoscale*, 2023, **15**, 2595

Nanostructured doping of WSe_2 *via* block copolymer patterns and its self-powered photodetector application

Miae Kang,†[a] Ki Hyun Kim,†[a] Joona Bang *[a] and Jihyun Kim *[b]

Received 2nd December 2022,
Accepted 23rd December 2022

DOI: 10.1039/d2nr06742k

rsc.li/nanoscale

Transition metal dichalcogenides (TMDs), *e.g.*, MoS_2, $MoSe_2$, ReS_2, and WSe_2, are effective materials for advanced optoelectronics owing to their intriguing optical, structural, and electrical properties. Various approaches for manipulating the surface of the TMDs have been suggested to unleash the optoelectronic potential of the TMDs. Herein, we employed the self-assembly of the poly(styrene-*b*-methyl methacrylate) (PS-*b*-PMMA) block copolymer (BCP) to prepare a nanoporous pattern and generate nanostructured charge-transfer p-doping on the WSe_2 surface, maximizing the depletion region in the absorber layer. After the spin coating and thermal annealing of PS-*b*-PMMA, followed by the selective etching of PMMA cylindrical microdomains using oxygen reactive-ion plasma, nanopatterned WO_x with high electron affinity was grown on the WSe_2 surface, forming a three-dimensional homojunction. The nanopatterned WO_x significantly expanded the depletion region in the WSe_2 layer, thus enhancing optoelectronic performance and self-powered photodetection. The proposed approach based on the nanostructured doping of the TMDs *via* BCP nanolithography can help create a promising platform for highly functional optoelectrical devices.

Published on 26 Desember 2022. Downloaded on 08/01/2026 10.46.26.

Introduction

Two-dimensional (2D)-layered materials, also known as van der Waals (vdW) materials, exhibit excellent potential in optical sensing applications owing to their tunable band-gaps, strong light–matter interactions, chemical/mechanical stability, and defect-free surface.[1–3] Transition metal dichalcogenides (TMDs), *e.g.*, MoS_2, $MoSe_2$, ReS_2, and WSe_2, as promising optoelectronic materials have garnered attention owing to their unique electrical and optical characteristics, including thickness-dependent absorption coefficient and high carrier mobility, enabling fast and wavelength-selective photodetection for high-responsivity broad-band applications.[4,5] In addition, TMD-based heterostructures, which are independent of lattice mismatches, allow versatile optoelectronic device architectures because heteroepitaxy in conventional semiconductors is restricted by the lattice constants between the neighboring layers.[6,7] Among various TMDs, WSe_2, which exhibits ambipolar transport characteristics with decent hole (~250 $cm^2\ V^{-1}\ s^{-1}$) and electron (~270 $cm^2\ V^{-1}\ s^{-1}$) mobilities, has been extensively investigated in the applications of field-effect transistors (FETs) and photodetectors owing to its large and tunable band-gap energy (monolayer (1.7 eV) and multilayer (1.2 eV)).[8,9] A high-gain WSe_2 complementary metal oxide semiconductor (CMOS) invertor with localized charge transfer doping has been demonstrated.[10] An infrared WSe_2-based photodetector with high sensitivity was reported with a vertical heterojunction structure between WSe_2 and black phosphorus.[11] To collect more electron–hole pairs (EHPs) efficiently generated by photon absorption, different device architectures have been proposed, including forming p–n homo-[12] or heterojunctions[13] and integrating with quantum dots,[59] polymers,[14] or perovskites.[15]

One of the challenges with TMDs is the development of facile and robust doping methods because conventional doping techniques, including high-temperature diffusion and high-energy ion implantation, are inappropriate for atomically thin layers.[16] A controllable doping process in a semiconductor is a fundamental building block that helps construct p–n junctions, where a built-in electric field can separate photo-generated EHPs.[17–19] As the exciton binding energy of the TMDs is relatively high, thermal energy is not sufficient to dissociate the bound excitons.[20,21] Interestingly, the WO_x layer with high electron affinity can be natively grown in WSe_2, enhancing hole conductivity in the underlying WSe_2.[22,23] Moreover, the ambipolarity of WSe_2 allows us to select the

[a]*Department of Chemical and Biological Engineering, Korea University, Seoul 02841, Republic of Korea. E-mail: joona@korea.ac.kr*
[b]*School of Chemical and Biological Engineering, Seoul National University, Seoul 08826, Republic of Korea. E-mail: jihyunkim@snu.ac.kr*
† These authors contributed equally to this work.

Published on 26 Desember 2022. Downloaded on 08/01/2026 10.46.26.

majority carrier type by applying electrostatic potential.[8] Various oxidation methods, *e.g.*, thermal annealing under oxygen ambient conditions,[24] mild oxygen plasma treatment,[25] and laser-induced oxidation,[12] have been studied; these methods demonstrate versatile lateral and vertical junctions. The WO_x layer can also behave as a surface protection layer, which is critical to ensure the stability of electronic devices, as 2D-material-based electronic devices have suffered from air instability.[26]

To further improve photon absorption, various surface treatments for TMDs have been introduced.[27–31] Kim *et al.* demonstrated that the responsivity of MoS_2 phototransistors can be enhanced by the fabrication of nanopatterns on multilayer (ML) MoS_2 TMDs using the self-assembly of block copolymers (BCPs).[27] BCPs are comprised of two or more chemically distinct polymers covalently bonded in a single chain and form various periodic nanostructures *via* microphase separation.[32–41] In this case, the hexagonally packed nanoarrays of the BCPs provided abundant exposed edges, which were responsible for multiple trap states in the band-gap region, which is crucial for the photogating effect. Herein, we fabricated nano-dot arrays on ML WSe_2 FETs using the self-assembly of a cylinder-forming poly(styrene-*b*-methyl methacrylate) (PS-*b*-PMMA) BCP. The selective etching of the PMMA microdomains *via* O_2 reactive ion etching (RIE) oxidized WSe_2 to WO_x, leading to the p-doping of WSe_2.[39] Consequently, the optoelectronic performance of ML WSe_2 FETs significantly improved. Moreover, it was confirmed that nanopatterned WSe_2 photodetectors can be operated without an external power source. The self-powered operation of a photodetector is favored because it is size-efficient and light. As the formation of the depletion region is critical to separate and collect photo-excited carriers, recent studies have been focusing on the construction of the depletion region using Schottky and p–n junctions. As Fermi-level pinning limits the engineering of Schottky barrier heights in TMDs, the formation of p–n homo- or heterojunctions has been alternatively investigated. We introduced the nanostructured doping of WSe_2 using a single-step BCP nanolithography process, demonstrating the three-dimensional (3D) WSe_2 homojunction photodetector with self-powered photodetection capability.

Experimental details

Fabrication of WSe_2 TFTs

Fig. 1 shows the fabrication process of the self-powered WSe_2 photodetector with the nanostructured 3D junction. WSe_2 flakes were mechanically exfoliated from the bulk single crystal (purchased from HQ graphene) using the conventional Scotch tape method. The exfoliated WSe_2 flakes were dry-transferred onto a SiO_2/p^{++}-Si substrate using a transparent polydimethylsiloxane film (Gel-Pak) and micromanipulator. The source and drain electrodes were defined on the WSe_2 flake using electron-beam lithography, and the Ti/Au electrodes (20/80 nm) were deposited using electron-beam evaporation. After the lift-off process, thermal annealing was performed under vacuum conditions (1×10^{-5} Torr) at 250 °C for 2 h to improve Ohmic behaviors and eliminate the bubbles trapped in the interface between the WSe_2 flake and the SiO_2 substrate.

Preparation of BCP nanoporous patterns

The PS-*b*-PMMA (M_{PS} = 57 kg mol^{-1}, M_{PMMA} = 25 kg mol^{-1}, M_w/M_n = 1.07) BCP was purchased from Polymer Source Inc. Meldrum's acid containing cross-linkable PS-*r*-PMMA random copolymers was synthesized using a previously reported method.[42] It consists of styrene (52 mol%), MMA (45 mol%), and Meldrum's acid (3 mol%), and the total number average molecular weight was 24 kg mol^{-1} (M_w/M_n = 1.13).[42] To obtain vertically oriented cylindrical nanopatterns on WSe_2 FETs, WSe_2 surfaces were neutralized with cross-linkable PS-*r*-PMMA random copolymers by spin-coating (3000 rpm, 45 s) 0.4 wt%

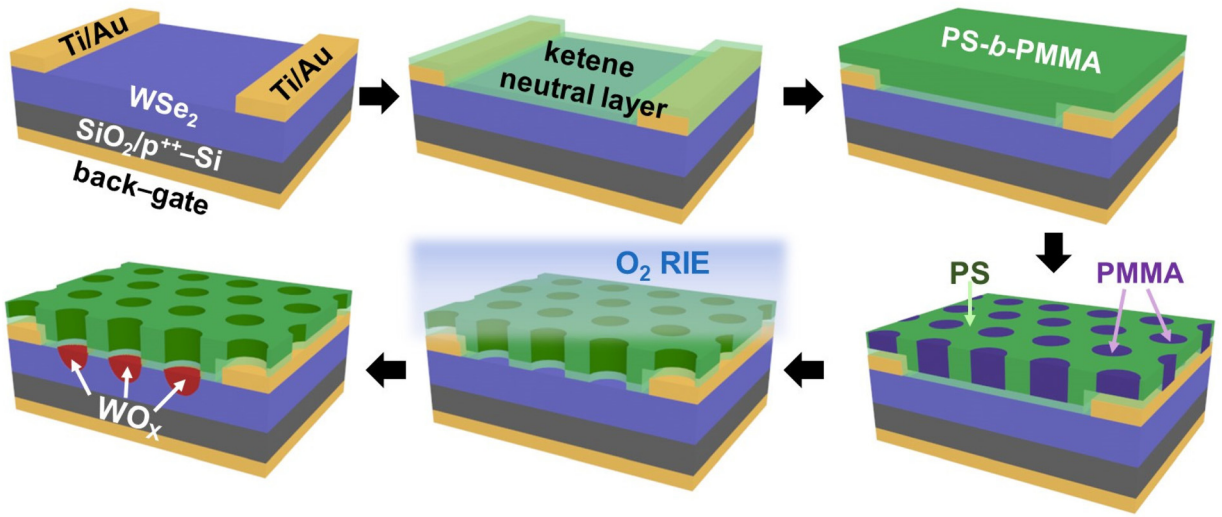

Fig. 1 Fabrication of the self-powered WSe_2 photodetector with the 3D nanostructured homojunction using the BCP nanolithography process.

 This journal is © The Royal Society of Chemistry 2023

Published on 26 Desember 2022. Downloaded on 08/01/2026 10.46.26.

toluene solution. Then, the PS-*r*-PMMA layer was thermally cross-linked at 230 °C for 1 h *in vacuo*. To prepare BCP films, 2 wt% toluene solution of PS-*b*-PMMA was prepared and spin-coated (3000 rpm, 45 s) on the WSe_2 substrate possessing a cross-linked neutral layer. Then, the BCP-coated WSe_2 FETs were thermally annealed at 210 °C for 24 h. To prepare nanoporous BCP templates, RIE was employed using O_2 with an RF power of 90 W at 20 sccm (Cute-1MP, Femto Science) to selectively remove PMMA microdomains and the underlying neutral layers. The etch rates were 0.81, 1.47, and 1.16 nm s^{-1} for PS, PMMA, and the cross-linked PS-*r*-PMMA neutral layer, respectively.

Characterization

The thicknesses of the cross-linked PS-*r*-PMMA neutral layers and PS-*b*-PMMA BCP films were measured using spectroscopic ellipsometry (SE MG-1000, Nano-view Co.) at an incidence angle of 70.2° based on the Cauchy model. An atomic force microscope (AFM, Park Systems NX-10) was used to determine the thickness of the WSe_2 flakes and characterize the BCP nanopatterns on the WSe_2 surfaces. Phase and Z-height profile data were obtained with non-contact mode settings. A field emission scanning electron microscope (FE-SEM) (JSM-6700F, JEOL) was employed to investigate the nanoporous BCP pattern on the WSe_2 flake. The optical properties of the WSe_2 flake before and after BCP patterning were characterized using micro-Raman spectroscopy under the back-scattering geometry with a diode-pumped solid-state laser (Omicron) of 532 nm wavelength. The optoelectronic properties were determined using a semiconductor parameter analyzer (Agilent 4155C) connected to a low-vacuum probe station (7.9 mTorr). The optical intensities of LED light sources (Newport) of 530 and 780 nm were calibrated using a power meter (FieldMaxII-TO, Coherent). An optical beam shutter (SHB1T, Thorlabs) connected to a pulse generator (Agilent 33250A) was used to analyze the time-dependent photoresponses of the fabricated photodetectors.

Results and discussion

To enhance the optoelectrical properties of the WSe_2 photodetector, nanoporous BCP patterns were prepared on the WSe_2 surfaces (Fig. 1). First, back-gated ML WSe_2 FETs were fabricated by transferring exfoliated WSe_2 flakes onto a SiO_2 substrate, followed by the deposition of Ti/Au electrodes. Then, cylinder-forming PS-*b*-PMMA BCP thin films were prepared on the WSe_2 surfaces with a film thickness of ~74 nm. To obtain nano-dot arrays, cylindrical PMMA microdomains need to be oriented perpendicularly to the substrate, and this can be accomplished using the ultrathin layer of the PS-*r*-PMMA random copolymer that neutralizes the WSe_2 surface.[42–52] In this study, we employed a cross-linkable PS-*r*-PMMA random copolymer containing Meldrum's acid, which generates reactive ketenes upon heating and forms a cross-linked neutral layer.[42] The BCP was spin-coated on the neutral layer and annealed at 210 °C. As shown in Fig. 2(c), hexagonally packed

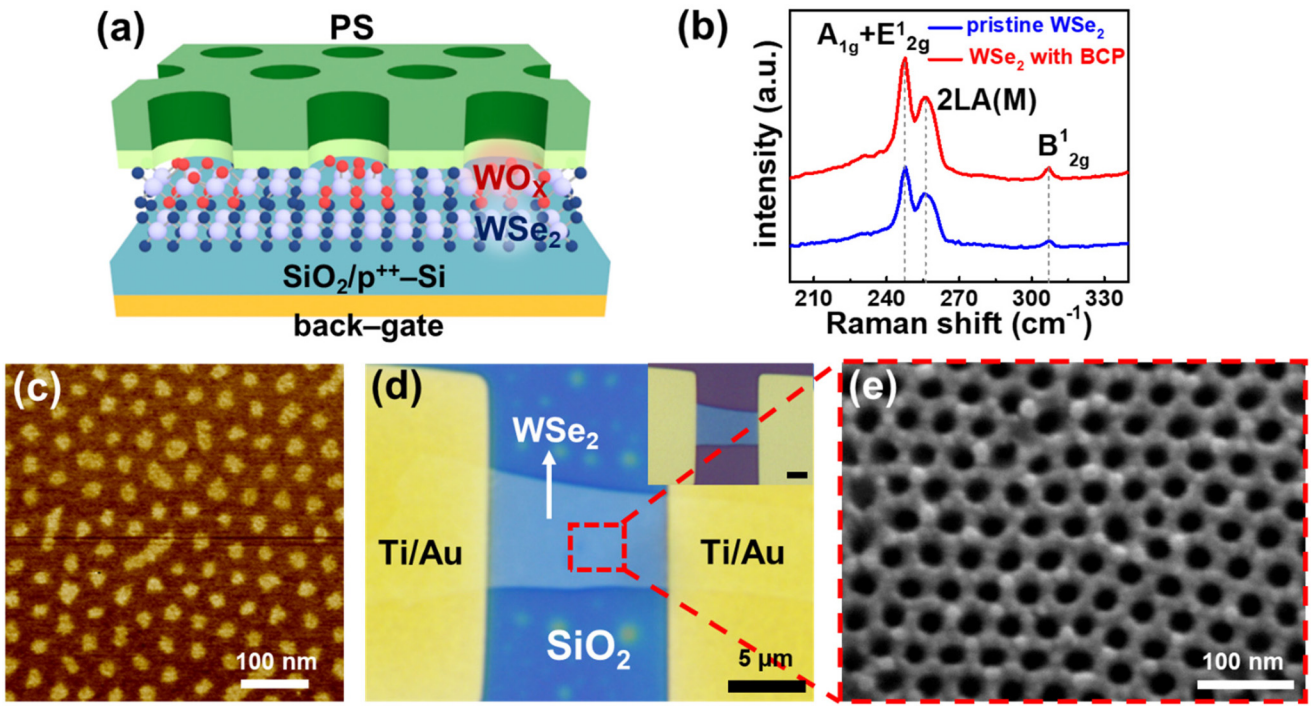

Fig. 2 (a) Schematic of the 3D WSe_2 homojunction with nanoporous PS. (b) Micro-Raman spectra of the pristine and BCP-patterned WSe_2. (c) AFM phase image of cylinder-forming PS-*b*-PMMA BCP thin films on the WSe_2 flake. (d) Optical microscopy of the WSe_2 photodetector. (e) SEM images of nanoporous BCP patterns on the WSe_2 photodetector.

Published on 26 Desember 2022. Downloaded on 08/01/2026 10.46.26.

nano-dot arrays are formed, indicating the vertically oriented PMMA cylinders. To generate nanoporous patterns, the PMMA microdomains were selectively removed using O_2 RIE with known etching rates of PS and PMMA (PS: 0.81 nm s^{-1}, PMMA: 1.47 nm s^{-1}). After the complete removal of PMMA and the underlying neutral layer, additional RIE was allowed for a few seconds to oxidize the exposed WSe_2, creating nanopatterned WO_x embedded on the WSe_2 surface. As shown in Fig. 2(e), the average diameter of the nanopore is 28 nm with a domain spacing of 40 nm.[53]

The oxygen plasma treatment during PMMA removal makes the underlying WSe_2 oxidized, forming the structure of WO_x/WSe_2 (Fig. 2(a)). As WO_x with a high work-function makes the neighboring WSe_2 electron-deficient, the underlying WSe_2 can be p-doped using the charge-transfer process.[23] The oxidation of WSe_2 has been intensively investigated using laser annealing,[54] oxygen plasma,[55] UV-ozone treatment,[56] and thermal annealing[24] under oxygen ambient conditions. Yang *et al.* effectively constructed seamless WSe_2 homojunction diodes by converting the top few layers of WSe_2 to WO_x ($x < 3$) *via* 325 nm laser exposure.[54] Moon *et al.* fabricated an oxidized WSe_2 FET with reduced channel resistance and a clean interface using the oxygen plasma treatment.[57] The oxidation of WSe_2, which is a self-limiting process, is initiated by substituting the Se vacancy with an oxygen atom; this is a spontaneous process with an enthalpy of −4.7 eV.[58] Micro-Raman spectroscopy confirms that the crystallinity of the underlying WSe_2 is well maintained after BCP patterning (Fig. 2(b)), although the oxidation process may create dangling bonds in the WSe_2 layer because the oxidation can proceed in the out-of-plane direction through the intrinsic defects. Fig. 2(d) shows the optical microscopy image of the ML WSe_2 photodetector possessing nanoporous BCP patterns. The SEM image of the nanoporous ML WSe_2 device indicates that the cylindrical PMMA microdomains are oriented perpendicularly to the WSe_2 surface, implying that the proposed single-step BCP nanolithography process is applicable for the post-fabrication process of TMD materials.

The current–voltage (I_{DS}–V_{DS}) characteristics of the nanoporous WSe_2 FETs at zero V_{GS} were compared under different illumination conditions as shown in Fig. 3(a) and (b). The low current levels can be attributed to the unwanted interface states and the non-optimization of the device layout. The EHPs were created using 530 and 780 nm wavelengths, generating photocurrents. The increase in the photocurrents was higher for the nanoporous WSe_2 FET owing to the formation of 3D

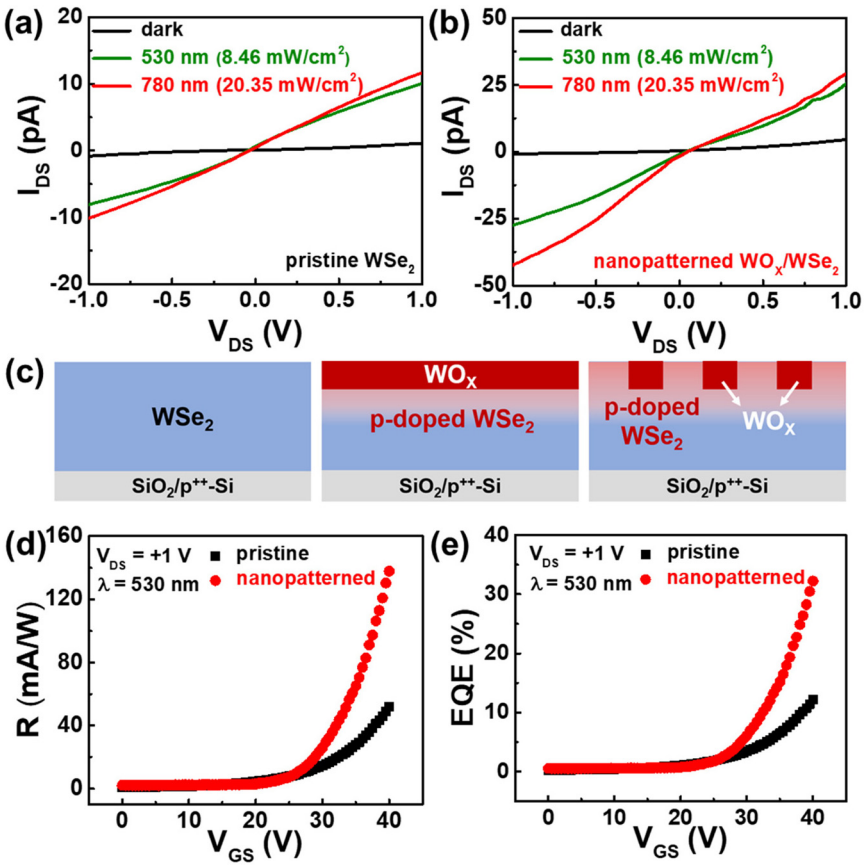

Fig. 3 Current–voltage characteristics of the (a) pristine and (b) nanopatterned WSe_2 device under different irradiation conditions (dark, and 530 nm and 780 nm wavelengths). (c) WSe_2 without a junction (left), WSe_2 with a planar junction (middle), and WSe_2 with a 3D nanostructured junction (right). (d) Responsivity (R) and (e) external quantum efficiency (EQE) at varying values of V_{GS}.

 This journal is © The Royal Society of Chemistry 2023

Published on 26 Desember 2022. Downloaded on 08/01/2026 10.46.26.

built-in electric fields (Fig. 3(c)). In pristine WSe_2, no electric fields exist, which is inefficient for collecting the generated EHPs under the exposure of light (Fig. 3c, left). Compared to the pristine one, the formation of layered WO_x can help develop 2D electric fields; it is a conventional method to form built-in electric fields (Fig. 3c, middle). In contrast, the nanopatterned BCP architecture can form 3D electric fields, which allows us to collect additional EHPs owing to the expansion of the depletion region (right side of Fig. 3(c)). The photons that were absorbed near and in the depletion region can help generate photocurrents.

Although the one-atom-thick TMD layer may achieve optimal electrical performance with a high on/off ratio and low power consumption, the lower optical absorption compared to the thick one limits its optoelectronic properties. As an alternative, the ML TMD layer is beneficial for optical absorbance. As the collection efficiency increases with the expansion of the depletion region, the photoresponse performances (responsivity (R) and external quantum efficiency (EQE)) were improved using the positive value of V_{GS} (Fig. 3(d) and (e)) under the illumination of 530 nm wavelength, implying the WO_x-induced p-doping of WSe_2. Operation in the increased depletion region under the appropriate gate bias caused the formation of the absorber layer, which is extremely sensitive to incoming photons through the channel. The optoelectronic parameters under the bias conditions of V_{DS} = +1 V and V_{GS} = 0 V are shown in Fig. 4(d). The responsivity (R) of the nanoporous WSe_2 photodetector was calculated using the following equation:

$$R = \frac{I_p}{A \cdot P},$$

where I_p denotes the photocurrent (defined as $I_{illumination} - I_{dark}$), A denotes the effective area, and P denotes the light power density. The external quantum efficiency (EQE) is defined by the following formula:

$$\mathrm{EQE} = \frac{hc}{e\lambda}R,$$

where h denotes the Planck constant, c denotes the speed of light, and λ denotes the wavelength of the illuminated light. The detectivity (D^*) and photo-to-dark current ratio (PDCR) were obtained using the following equations:

$$D^* = \frac{RA^{0.5}}{(2q \cdot I_{dark})^{0.5}},$$

$$\mathrm{PDCR} = \frac{I_{illumination} - I_{dark}}{I_{dark}} \times 100$$

where q denotes the electronic charge. The dynamic photoresponse characteristics of WSe_2 photodetectors were compared with and without BCP nanopatterns. As shown in Fig. 4(a) and (b), time-dependent photocurrents were measured at varying intensities of 530 nm wavelength. The photocurrents increased with an increase in the light intensity, which indicates the high quality of the WO_x/WSe_2 structure (Fig. 4(c)). The optoelectronic performances significantly improved after BCP patterning on WSe_2 with fast response and decay characteristics. Persistent photoconductivity (PPC) was not observed, indicating that BCP patterning induced nominal defects in WSe_2. The self-powered photodetection mechanism of the nanoporous WSe_2 photodetector illustrated in Fig. 5(a) was demonstrated, where high photocurrents were obtained after BCP patterning (Fig. 5(b)). The negligible photocurrent

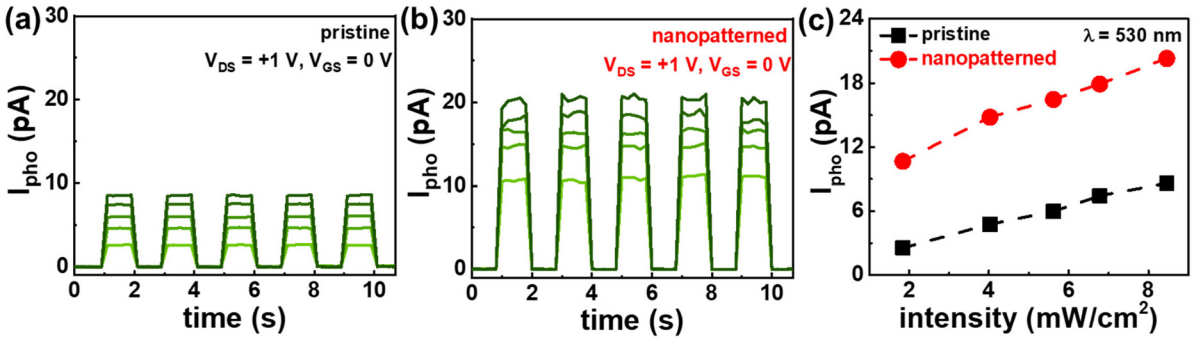

(d)

parameter	pristine WSe_2	nanopatterned WO_x/WSe_2
photocurrent (pA)	2.56	10.7
R (mA/W)	1.76	7.35
PDCR	4.65	12.3
D* (jones)	3.73×10^9	1.23×10^{10}
EQE (%)	0.413	1.72

Fig. 4 Time-dependent photocurrent characteristics of the (a) pristine and (b) nanopatterned WSe_2 photodetector at varying optical intensities (530 nm wavelength). (c) Photocurrent at different optical intensities. (d) Optoelectronic parameters under the bias conditions of V_{DS} = +1 V and V_{GS} = 0 V considering the exposure of 530 nm with a light power density of 1.8 mW cm^{-2}.

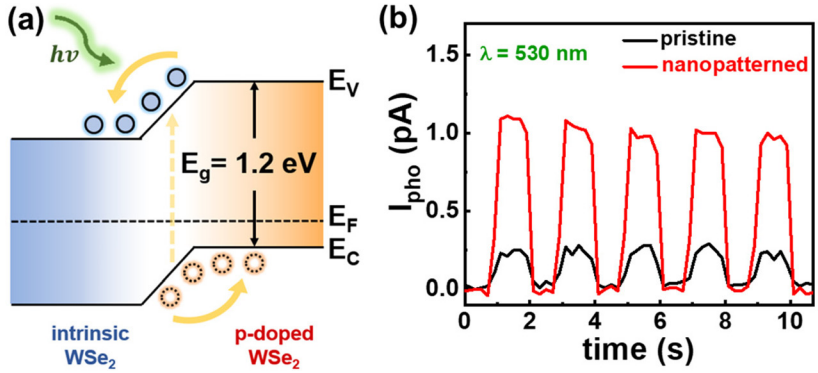

(c)

parameter	pristine	nanopatterned
I_{pho} (pA)	0.23	1.09
R (mA/W)	0.034	0.164
PDCR	3.3	109
D* (jones)	8.01×10^{7}	2.52×10^{9}
EQE (%)	0.0081	0.0383

Fig. 5 (a) Mechanism of the self-powered WSe_2 photodetector. (b) Time-dependent photocurrent characteristics. (c) Optoelectronic performances of the pristine and nanopatterned WSe_2.

Published on 26 Desember 2022. Downloaded on 08/01/2026 10.46.26.

obtained from the pristine WSe_2 photodetector can be attributed to the non-ideal Ohmic contact with WSe_2 caused by Fermi-level pinning. The performance of the self-powered WSe_2 photodetector is illustrated in Fig. 5(c). Among the different methods to form built-in electric fields, including Schottky contacts, the p–n homojunction, and the p–n heterojunction, the p–n homojunction can be ideal because it nominally affects the absorber layer. Self-powered photodetectors can be miniaturized because they do not require external power sources.

Conclusion

A 3D homojunction was demonstrated in WSe_2 using a one-step BCP nanolithography process, enabling an effective collection of EHPs. The oxygen plasma used to remove PMMA cylindrical microdomains in PS-*b*-PMMA thin films oxidized the underlying WSe_2, forming a 3D WO_x/WSe_2 structure. The current–voltage output and transfer characteristics based on the fabricated WO_x/WSe_2 FET were obtained under dark and different illumination conditions, confirming the formation of built-in electric fields. The optoelectronic performances, including responsivity, PDCR, detectivity, and EQE, were significantly improved owing to the introduction of the multidimensional homojunction structure. There was no PPC at varying light power, implying a high-quality interface. Self-powered photodetection, which can operate without an external power source, was demonstrated with excellent static and dynamic photosensing performance. This study can provide a pathway for the development of high-performance stand-alone photodetectors based on the multidimensional device architecture.

Conflicts of interest

There are no conflicts to declare.

Acknowledgements

This work was supported by a National Research Foundation of Korea (NRF) grant funded by the Korean government (MSIT) (No. 2020M3H4A3081799 and 2022R1A4A1020543) and the K-Sensor Development Program (No. RS-2022-00154729), funded by the Ministry of Trade, Industry and Energy (MOTIE, Korea).

References

1 F. Yan, Z. Wei, X. Wei, Q. Lv, W. Zhu and K. Wang, *Small Methods*, 2018, **2**, 1700349.
2 C. Liu, J. Guo, L. Yu, J. Li, M. Zhang, H. Li, Y. Shi and D. Dai, *Light: Sci. Appl.*, 2021, **10**, 123.
3 C. Xie, C. Mak, X. Tao and F. Yan, *Adv. Funct. Mater.*, 2017, **27**, 1603886.
4 M. Long, P. Wang, H. Fang and W. Hu, *Adv. Funct. Mater.*, 2019, **29**, 1803807.
5 T. Tan, X. Jiang, C. Wang, B. Yao and H. Zhang, *Adv. Sci.*, 2020, **7**, 2000058.
6 K. S. Novoselov, A. Mishchenko, A. Carvalho and A. H. Castro Neto, *Science*, 2016, **353**, aac9439.
7 F. Wang, K. Pei, Y. Li, H. Li and T. Zhai, *Adv. Mater.*, 2021, **33**, 2005303.
8 S. Das and J. Appenzeller, *Appl. Phys. Lett.*, 2013, **103**, 103501.
9 Z. Jin, X. Li, J. T. Mullen and K. W. Kim, *Phys. Rev. B: Condens. Matter Mater. Phys.*, 2014, **90**, 045422.
10 L. Yu, A. Zubair, E. J. Santos, X. Zhang, Y. Lin, Y. Zhang and T. Palacios, *Nano Lett.*, 2015, **15**, 4928–4934.
11 L. Ye, P. Wang, W. Luo, F. Gong, L. Liao, T. Liu, L. Tong, J. Zang, J. Xu and W. Hu, *Nano Energy*, 2017, **37**, 53–60.
12 J. Chen, Q. Wang, Y. Sheng, G. Cao, P. Yang, Y. Shan, F. Liao, Z. Muhammad, W. Bao and L. Hu, *ACS Appl. Mater. Interfaces*, 2019, **11**, 43330–43336.
13 H. Xue, Y. Wang, Y. Dai, W. Kim, H. Jussila, M. Qi, J. Susoma, Z. Ren, Q. Dai and J. Zhao, *Adv. Funct. Mater.*, 2018, **28**, 1804388.

 This journal is © The Royal Society of Chemistry 2023

Published on 26 Desember 2022. Downloaded on 08/01/2026 10.46.26.

14 M. H. Jeong, H. S. Ra, S. H. Lee, D. H. Kwak, J. Ahn, W. S. Yun, J. Lee, W. S. Chae, D. K. Hwang and J. S. Lee, *Adv. Mater.*, 2022, **34**, 2108412.
15 J. Lu, A. Carvalho, H. Liu, S. X. Lim, A. H. Castro Neto and C. H. Sow, *Angew. Chem.*, 2016, **128**, 12124–12128.
16 P. Luo, F. Zhuge, Q. Zhang, Y. Chen, L. Lv, Y. Huang, H. Li and T. Zhai, *Nanoscale Horiz.*, 2019, **4**, 26–51.
17 X. Yu, S. Zhang, H. Zeng and Q. J. Wang, *Nano Energy*, 2016, **25**, 34–41.
18 Z.-Q. Xu, Y. Zhang, Z. Wang, Y. Shen, W. Huang, X. Xia, W. Yu, Y. Xue, L. Sun and C. Zheng, *2D Mater.*, 2016, **3**, 041001.
19 J. Wang, J. Han, X. Chen and X. Wang, *InfoMat*, 2019, **1**, 33–53.
20 J. Huang, T. B. Hoang and M. H. Mikkelsen, *Sci. Rep.*, 2016, **6**, 22414.
21 T. Mueller and E. Malic, *npj 2D Mater. Appl.*, 2018, **2**, 29.
22 J. Meyer, S. Hamwi, M. Kröger, W. Kowalsky, T. Riedl and A. Kahn, *Adv. Mater.*, 2012, **24**, 5408–5427.
23 M. Yamamoto, S. Dutta, S. Aikawa, S. Nakaharai, K. Wakabayashi, M. S. Fuhrer, K. Ueno and K. Tsukagoshi, *Nano Lett.*, 2015, **15**, 2067–2073.
24 Y. Liu, C. Tan, H. Chou, A. Nayak, D. Wu, R. Ghosh, H.-Y. Chang, Y. Hao, X. Wang and J.-S. Kim, *Nano Lett.*, 2015, **15**, 4979–4984.
25 Y. C. Lin, B. M. Bersch, R. Addou, K. Xu, Q. Wang, C. M. Smyth, B. Jariwala, R. C. Walker, S. K. Fullerton-Shirey and M. J. Kim, *Adv. Mater. Interfaces*, 2020, **7**, 2000422.
26 M. Yamamoto, S. Nakaharai, K. Ueno and K. Tsukagoshi, *Nano Lett.*, 2016, **16**, 2720–2727.
27 H. Park, J. Lee, G. Han, A. AlMutairi, Y.-H. Kim, J. Lee, Y.-M. Kim, Y. J. Kim, Y. Yoon and S. Kim, *Commun. Mater.*, 2021, **2**, 94.
28 H. Xue, Y. Dai, W. Kim, Y. Wang, X. Bai, M. Qi, K. Halonen, H. Lipsanen and Z. Sun, *Nanoscale*, 2019, **11**, 3240–3247.
29 G. Nazir, M. F. Khan, I. Akhtar, K. Akbar, P. Gautam, H. Noh, Y. Seo, S.-H. Chun and J. Eom, *RSC Adv.*, 2017, **7**, 16890–16900.
30 C. Chen, H. Qiao, S. Lin, C. M. Luk, Y. Liu, Z. Xu, J. Song, Y. Xue, D. Li and J. Yuan, *Sci. Rep.*, 2015, **5**, 11830.
31 S. Qiao, R. Cong, J. Liu, B. Liang, G. Fu, W. Yu, K. Ren, S. Wang and C. Pan, *J. Mater. Chem. C*, 2018, **6**, 3233–3239.
32 J. Bang, U. Jeong, D. Y. Ryu, T. P. Russell and C. J. Hawker, *Adv. Mater.*, 2009, **21**, 4769–4792.
33 L. Leibler, *Macromolecules*, 1980, **13**, 1602–1617.
34 F. S. Bates and G. H. Fredrickson, *Annu. Rev. Phys. Chem.*, 1990, **41**, 525–557.
35 R. A. Segalman, *Mater. Sci. Eng., R*, 2005, **48**, 191–226.
36 C. J. Hawker and T. P. Russell, *MRS Bull.*, 2005, **30**, 952–966.
37 T. P. Russell, R. P. Hjelm Jr. and P. A. Seeger, *Macromolecules*, 1990, **23**, 890–893.
38 T. Xu, H.-C. Kim, J. DeRouchey, C. Seney, C. Levesque, P. Martin, C. Stafford and T. Russell, *Polymer*, 2001, **42**, 9091–9095.
39 A. Menelle, T. Russell, S. Anastasiadis, S. Satija and C. Majkrzak, *Phys. Rev. Lett.*, 1992, **68**, 67.
40 H. C. Kim and T. P. Russell, *J. Polym. Sci., Part B: Polym. Phys.*, 2001, **39**, 663–668.
41 T. P. Russell and Y. Chai, *Macromolecules*, 2017, **50**, 4597–4609.
42 H. Jung, F. A. Leibfarth, S. Woo, S. Lee, M. Kang, B. Moon, C. J. Hawker and J. Bang, *Adv. Funct. Mater.*, 2013, **23**, 1597–1602.
43 D. Y. Ryu, K. Shin, E. Drockenmuller, C. J. Hawker and T. P. Russell, *Science*, 2005, **308**, 236–239.
44 D. Y. Ryu, J.-Y. Wang, K. A. Lavery, E. Drockenmuller, S. K. Satija, C. J. Hawker and T. P. Russell, *Macromolecules*, 2007, **40**, 4296–4300.
45 H. Jung, D. Hwang, E. Kim, B.-J. Kim, W. B. Lee, J. E. Poelma, J. Kim, C. J. Hawker, J. Huh and D. Y. Ryu, *ACS Nano*, 2011, **5**, 6164–6173.
46 H. S. Wang, K. H. Kim and J. Bang, *Macromol. Rapid. Commun.*, 2019, **40**, 1800728.
47 S. H. Kim, M. J. Misner and T. P. Russell, *Adv. Mater.*, 2008, **20**, 4851–4856.
48 P. Mansky, Y. Liu, E. Huang, T. Russell and C. Hawker, *Science*, 1997, **275**, 1458–1460.
49 E. Huang, L. Rockford, T. Russell and C. Hawker, *Nature*, 1998, **395**, 757–758.
50 S. Ham, C. Shin, E. Kim, D. Y. Ryu, U. Jeong, T. P. Russell and C. J. Hawker, *Macromolecules*, 2008, **41**, 6431–6437.
51 S. Park, J.-Y. Wang, B. Kim, J. Xu and T. P. Russell, *ACS Nano*, 2008, **2**, 766–772.
52 E. Huang, S. Pruzinsky, T. Russell, J. Mays and C. Hawker, *Macromolecules*, 1999, **32**, 5299–5303.
53 H. S. Wang, A. Khan, Y. Choe, J. Huh and J. Bang, *Macromolecules*, 2017, **50**, 5025–5032.
54 S. Yang, G. Lee, J. Kim, S. Yang, C.-H. Lee and J. Kim, *J. Mater. Chem. C*, 2020, **8**, 8393–8398.
55 Z. Li, S. Yang, R. Dhall, E. Kosmowska, H. Shi, I. Chatzakis and S. B. Cronin, *ACS Nano*, 2016, **10**, 6836–6842.
56 D. Lee, Y. Choi, J. Kim and J. Kim, *ACS Nano*, 2022, **16**, 8484–8492.
57 I. Moon, S. Lee, M. Lee, C. Kim, D. Seol, Y. Kim, K. H. Kim, G. Y. Yeom, J. T. Teherani and J. Hone, *Nanoscale*, 2019, **11**, 17368–17375.
58 J. Lu, A. Carvalho, X. K. Chan, H. Liu, B. Liu, E. S. Tok, K. P. Loh, A. H. Castro Neto and C. H. Sow, *Nano Lett.*, 2015, **15**, 3524–3532.
59 D.-H. Kwak, P. Ramasamy, Y.-S. Lee, M.-H. Jeong and J.-S. Lee, *ACS Appl. Mater. Interfaces*, 2019, **11**, 29041–29046.